Design and manufacture of a large field of view thermal infrared catoptric imaging system in an αZ configuration

Louis Duveau, Guillaume Druart, Thierry Lepine

Research Article Vol. 31, No. 16 / 31 Jul 2023 / Optics Express 26659
Optics EXPRESS

Design and manufacture of a large field of view thermal infrared catoptric imaging system in an αZconfiguration

LOUIS DUVEAU,[1,*] GUILLAUME DRUART,[1] AND THIERRY LEPINE[2]

[1] ONERA-The French Aerospace Lab, 91123 Palaiseau Cedex, France
[2] Univ Lyon, Laboratory Hubert Curien, CNRS UMR 5516, 41000 Saint-Etienne, France
[*] louis@duveau.eu

Abstract: A geometry of a catoptric imaging system using three mirrors in an AlphaZ configuration is presented. This geometry allows large field of view and large aperture catoptric systems, useful for optronic pods as an example. A proof of concept with an 18×24 degree full field of view and a F/1.5 aperture is built using slow tool servo and 5 axis machining and characterized in the long wave infrared domain. The built system achieves nearly diffraction limited performance.

1. Introduction

In aerospace applications, the recent developments aim to reduce the allocated volume for optical instruments. The compactness of optical designs is critical to reduce the size and volume of the payloads. Such reduction effectively reduces the cost and complexity of scientific missions. The aerospace applications are numerous for lightweight and compact imaging instruments. Those compact geometries recently published extensively use freeform surfaces, as shown in the examples given in this introduction. Freeform surfaces are defined as surfaces that are not rotationnally symmetric nor a decentered part of a rotationnally symmetric surface [1]. In catoptric system the use of freeform surfaces allows an increase in optical performance, an increase of the field of view (FOV) and a decrease of the F-number of obscuration-free reflective systems [2,3]. This allows compact and well corrected off axis reflective designs [4]. Reflective designs have the advantage of being light, achromatic, and potentially low-cost due to cheaper materials involved. It could result in industrial production of compact panchromatic systems for various applications ranging from automotive sensors to imaging cubesats or optronic pods. In literature, those designs are mostly based on the three mirror anastigmat (TMA) geometry [5]. A minimal number of three mirrors is needed to perform imagery on a rectangular detector, as shown by Volatier et al. [6] in their study of the two mirror off axis solution space. An example of such TMA compatible with uncooled thermal imagery is shown in article from Zhu et al. [7]. Such designs are particularly useful as the TMA have been described as the best planar symmetric design for minimizing the aberrations using freeform surfaces [8,9]. TMA have been widely studied and used in recent years for compact designs, such as the TMA for the Proba-V mission [10] or the freeform TMAs for the MicroCarb mission [11].

The TMA design proved to be useful for most unobstructed optical designs, where the Y field of view remains around 10 degrees or lower. In this article, the Y field of view refers to the field of view of the system along a direction in the plane of symmetry of the system, and the X field of view is the field of view along the normal of this plane. Our goal however is to design a large FOV (18×24 degrees) and large aperture (F/1.5) system for uncooled long wave infrared (LWIR) imagery systems. To further increase the Y field of view in a catoptric system, the decenter of the mirrors must be increased, up to a point where the comparison with the systems of the study

#494194 https://doi.org/10.1364/OE.494194
Journal © 2023 Received 26 Apr 2023; revised 12 Jun 2023; accepted 13 Jun 2023; published 26 Jul 2023

Optics EXPRESS

of Bauer et al. [8] or Papa et al. [9] do not hold. Indeed, if we intend to increase the field of view with fixed aperture the tilts of the surfaces must be increased, leading to very strong nodal aberrations that are hard to correct. Such aberrations cause either a degradation of the root mean square (RMS) spot radius and needs very large departure from the best fit sphere to be only partially corrected [12]. This is mostly true for the Y FOV, as ultrawide X FOV systems have been designed using the TMA geometry [13]. A solution is to reduce the aperture, which is not possible in our case due to the requirements for uncooled long wave infrared (LWIR) imaging, or to change the configuration. For larger Y FOV, there are large FOV TMA that have been designed [14], the large field capability being ensured by the first two mirrors being used in an off axis Schwarzschild configuration. However, this wide field TMA is known to be particularly bulky.

As it happens, the use of freeform surfaces allows to extend the space of solutions and permits the use of more exotic configurations. Nakano et al. [15] demonstrated that a configuration in a circular shape can be more compact than a classical TMA and adapted to large aperture. This configuration has been later named the pamplemousse configuration [3,16–18]. In such configuration increasing the field of view do not affect the decenters and tilts as severely. However the pamplemousse configuration has several drawbacks, the main being the straylight management. This article first presents the geometry classification in use for this article. Then a study of a fast wide field of view design based on a pamplemousse configuration is presented, demonstrating the interest of such folded configuration for uncooled thermal infrared imaging. The third section presents a design based on the αZ geometry, which is the configuration B in the article from Bauer et al. [8]. A system based on this geometry is optimized for the same applications and presents several advantages over the pamplemousse configuration. The advantages are a longer back focal length, and total specular straylight rejection with smaller baffles. Finally, the last section shows the manufacturing and characterization of a first prototype based on this configuration for thermal infrared imaging.

2. Three mirror geometry classification

In this article, emphasis is made on design geometries. This is a topic frequently discussed [8,9,19]. We will use an extension of the geometry notations from Volatier et al. [6]. In this article, three main geometries using two mirrors are described. The three geometries are the U, Z and α geometries. They are described below:

1. The U geometry is given with same sign tilts of both mirrors. This geometry also implies that there is no crossing of the incoming beam with the output beam. This geometry is shown in Fig. 1(a).

2. The α geometry is also defined by same sign tilts for both mirrors. However, this geometry involves a crossing between the incoming beam and the output beam. This geometry is visible in Fig. 1(b).

3. The Z geometry is defined by opposite signs tilts for both mirrors. The geometry is shown in Fig. 1(c).

Each configuration can be easily identified by looking at the parabasal ray path, which is the chief ray for the central field. This classification has the advantage to be easily expanded to a larger number of mirrors if the system remains planar symmetric. Most configurations can be defined by finding the classification of successive pairs of mirrors. As an example, the TMA geometry shown in Fig. 2(a) is a ZZ configuration, the pamplemousse configuration is an $\alpha\alpha$, as shown in Figure 2(b). The αZ configuration differs from the pamplemousse from the positioning of the detector regarding the secondary mirror as shown in Fig. 2(c). The αZ configuration selected is the configuration b in the article from Bauer et al. [8]. The configuration c in the same

Optics EXPRESS

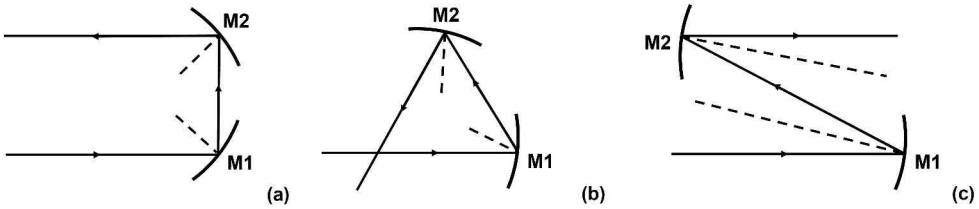

Fig. 1. (a):U geometry with two mirrors. (b):α geometry with two mirrors. (c):Z geometry with two mirrors.

reference is also an αZ configuration, but without crossing between the first and last sections of the parabasal ray path. A more complete method to describe geometries is given in article [20].

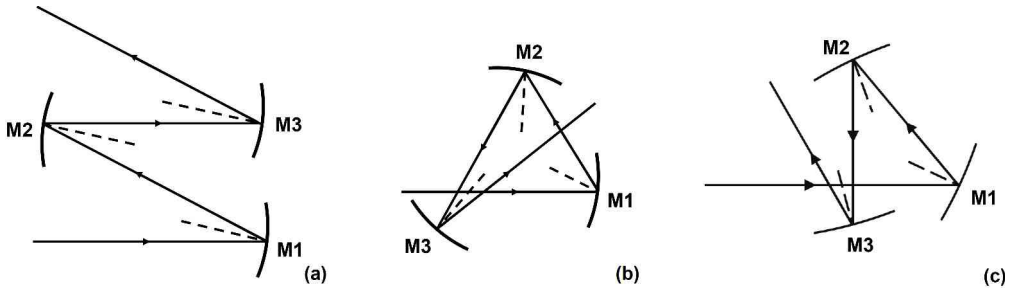

Fig. 2. (a):ZZ (or TMA) configuration. (b):$\alpha\alpha$ (or pamplemousse) configuration. (c):αZ configuration.

3. Design strategy

In this article the design method is as follows for each design. First, an on axis design with only spherical surfaces is generated. At this point, the focal length is fixed, but the field of view and aperture is greatly reduced. Tilts are then added to be compliant with the desired geometry. To avoid degeneracy [21], that comes with redundancy between the tilt in the surface definition and the tilt of the whole surface, the local slope at the center of each mirror is kept at zero so that the parabasal ray exactly hits each mirror at its center. We call this method the parabasal ray tracking and it helps the designer to keep control on the design. With this method a modification of the first surface will not move the beam location on subsequent mirrors. The effects of degeneracy are discussed in the study of Takaki et al. At this step, the merit function is completed to add geometrical constraints to avoid vignetting. This allows to let tilts and thicknesses between surfaces as variables.

At this point, the surfaces being spheres, the nodal aberrations are very strong and the point spread function is very large, usually several millimeters. The addition of freeform surfaces up to the third order allows to reduce these aberrations up to a point where the design is diffraction limited after optimization. The freeform polynomials chosen are the XY polynomials, as this is an easy solution for parabasal ray tracking, the local slope at the mirror center being conveniently only dependent on X and Y polynomials that are therefore fixed at zero. The X^2 polynomial is also kept at zero to avoid degeneracy between the radius of curvature and the sum $X^2 + Y^2$. Finally, the aperture and field of view are progressively increased until the specifications are met. Progressive increase in the number of freeform variables may be required. In this article, all design are specified up to the fifth order. TMA designs using this design strategy can be seen in our previous work [12,22].

Optics EXPRESS

4. Study of a fast wide field of view $\alpha\alpha$ configuration, or pamplemousse configuration

As explained in the introduction, the TMA is considered as the best three mirror catoptric solution [8,9,23]. However, these studies do not include designs with a large Y field of view, notably because the mirrors dimensions and departure from the best fit sphere become very large. In article [8] the pamplemousse configuration is described as a worst case scenario for the optimization of imaging optics. This fact has however only been shown for small fields of view where classical TMA configurations are known to be most efficient. As the pamplemousse configuration involves large decenters and tilts of optical surfaces for any field angle and aperture, the nodal aberrations are natively greater than for configurations with less tilted mirrors. However, this does not mean that the configuration is of no use. Indeed, if the aberrations can be lowered enough by the use of freeform surfaces, the configuration could actually be used for imaging purposes as demonstrated by Fuerschbach et al. [17]. Intuitively, the drawbacks of using this configuration should lower as the field increases due to the fact that the tilts and decenters do not vary much with the FOV in the pamplemousse configuration. To test this assumption, several pamplemousse with increasing FOV and decreasing F number have been designed. The final design obtained is a system with a FOV of 24×18 degrees and a F number of 1.5. The specifications are given in Table 1. The layout of the design is given in Fig. 3(a) and the RMS spot radius of the system is given in Fig. 3(b). This shows the theoretical feasability of such designs for large Y FOV and compatibility with uncooled LWIR imagery.

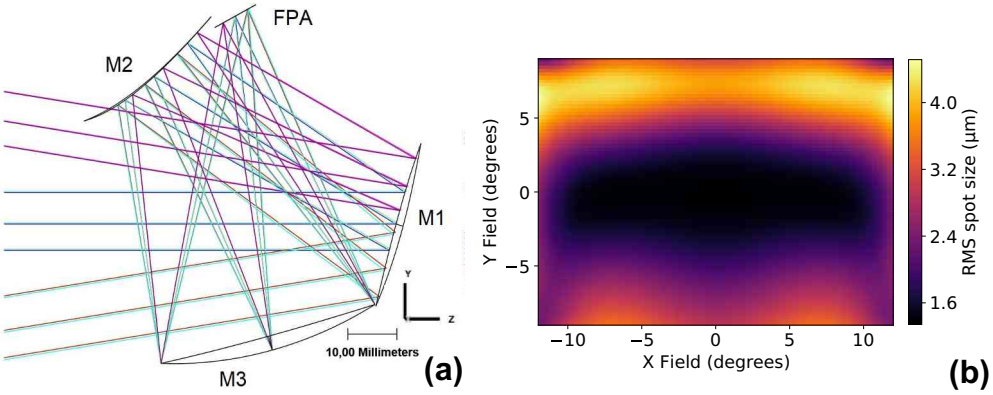

Fig. 3. (a):Pamplemousse design with a 24x18 FOV, F#1.5. (b):RMS spot radius over the FOV of the pamplemousse from subfigure (a). Mean RMS spot radius = 2.5μm.

Table 1. Specifications of the large FOV pamplemousse

Specification	Value
focal length	18 mm
half X FOV	12 degrees
half Y FOV	9 degrees
F#	1.5
pupil position	M3

However, decreasing the F number and increasing the FOV reduces the back focal length of the design, and the focal plane array gets close to the secondary mirror and to the rays coming from the entrance aperture. In this configuration, the detector is naturally placed in front of the

Optics EXPRESS

entrance aperture, as it lies between the first and second mirrors, in the top right area of Fig. 4. This leads to added risk of direct straylight paths or specular straylight via reflections on the mirrors M1 and M3 as shown in Fig. 4.

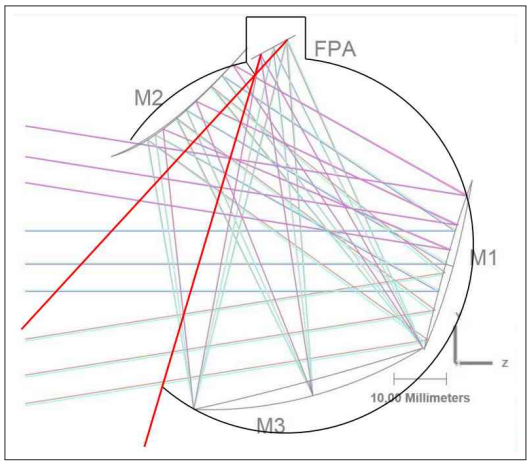

Fig. 4. Direct strayligh path for the pamplemousse configuration.

To avoid specular and direct straylight, the detector position has to been changed in a way that places the focal plane in a position that can not be seen from the entrance aperture.

5. Study of a fast wide field of view αZ configuration

In this section, we study the αZ configuration. In order to assess the interest of this configuration for large field of view and large aperture imaging systems, we designed a system using this configuration with the same specifications, given in Table 1.

5.1. Design of the αZ system

Fig. 5(a) shows an αZ with the same specifications as the large FOV pamplemousse from Fig. 3(a). The RMS spot radius over the field of view is shown in Fig. 5(b). The design is diffraction limited over the whole FOV in thermal infrared. Indeed at 10 microns, the airy radius is 18.3 micrometers, which is far more than the maximal RMS spot radius in Fig. 5(b).

Figure 6 shows the principal interest of this configuration. First, to avoid direct illumination of the detector, this configuration places the detector close to the entrance aperture and with an angle such that straylight cannot reach the detector from the entrance aperture [24]. This effectively reduces the angle from where straylight can directly reach the detector. In Fig. 6, this angle is pictured by the two red rays, limited as much as possible by a baffle on the top of the figure. This angle can be compared to the same angle for the pamplemousse, pictured in Fig. 4. To remove this straylight path, a baffle must be added for both configurations but this baffle would be way smaller for the Alpha-Z design, effectively reducing the overall volume of the complete system.

Moreover, the placement of the detector allows the designer to use the secondary mirror and its mount as a natural baffle, preventing any ray coming from the first mirror to reach the focal plane array, as shown with the green line in the Fig. 6. As the focal plane is behind the secondary mirror, the rays reflected onto this mirror can neither reach the sensible area. A non sequential ray tracing has been performed on this design too to verify if there is a straylight path involving the third mirror. It results that the angle of the M3 ensures that there is no straylight path from a single reflection onto the third mirror. The non sequential ray tracing also allows to ensure that,

Optics EXPRESS

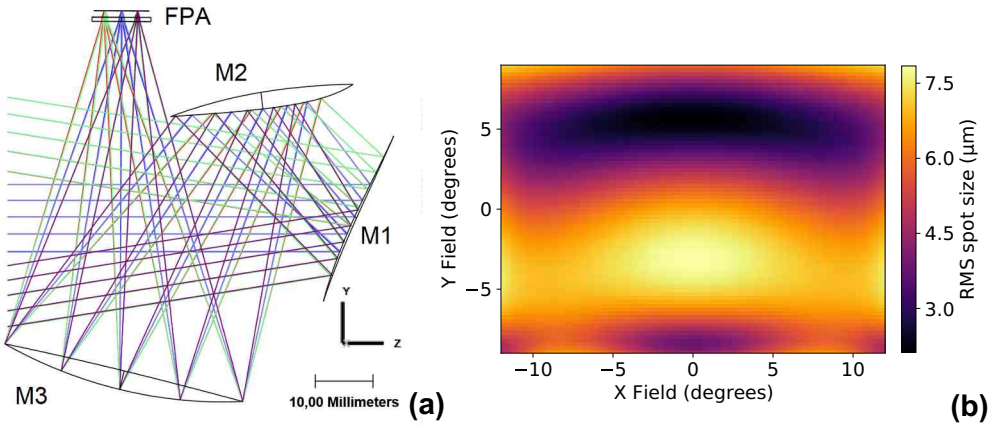

Fig. 5. (a):αZ design with a 24x18 FOV, F#1.5. (b):RMS field map of the αZ from subfigure (a). Mean RMS spot radius = 5.4μm.

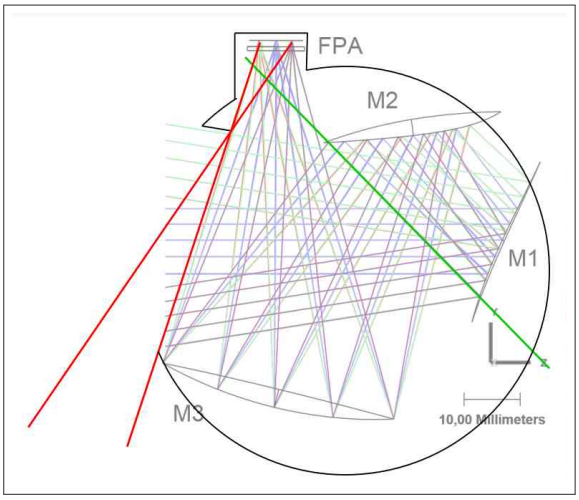

Fig. 6. Direct strayligh path for the αZ configuration.

in fine, there is no specular straylight in this system. Four billions rays have been traced from the detector in the direction of the third mirror with a cosine distribution large enough to cover the whole exit pupil from any point of the detector and not a single one reached the object space without being a ray from the useful FOV taking the nominal path (M3-M2-M1). Finally, another advantage of this design is that in the first optimization steps, the optimal tilt of the detector was found to be close to zero, so we could lock the design with no camera tilt, which simplifies the alignment process. All those features are not present in the Pamplemousse configuration, leading to straylight paths from single reflections on both the first and third mirrors. Overall, the Pamplemousse shows poor specular straylight management while the αZ configuration is naturally well suited to avoid specular straylight.

Finally, the αZ design presents a longer back focal length than the Pamplemousse design, which could be useful to add a beamsplitter to create a multi spectral bands optical instrument in future developments.

Optics EXPRESS

5.2. Tolerancing of the αZ configuration design

In classical optical design using rotationnaly symmetric surfaces, the design lies around an optical axis. Using this property the alignment is often simplified. In off axis optical design, the alignment is purely three dimensional, which creates added alignment complexity. In such configurations, the angular alignment of any mirror can become critical. To align correctly the system all mirrors must be placed in the right configuration, which can require either a long process and/or precise support equipment to align these mirrors. In this design, a tolerancing of the system misalignments has been performed with standard mechanical tolerances. The goal was to determine if the system could be manufactured without adjustment of the mirrors tilts and positions. To ensure that this was feasible, a tolerancing was performed, with the tolerances given in Table 2. The compensators selected are only the X,Y, and Z position of the detector. Such tolerances are comparable to the tolerances given in the article from Fuerschbach et al. [17]. Tolerances are applied using a Gaussian probability distribution and the given values are twice the standard deviation. No tolerancing of the manufacturing of optical surfaces has been performed due to a lack of feedback from the manufacturer and literature. As shown in the results in Table 3, the RMS spot radius should remain lower than the Airy pattern radius in the infrared spectrum with only the alignment of the focal plane array.

Table 2. Alignment tolerances (the tolerance applies to all three mirrors)

Specification	Value
positioning (X,Y)	100 μm
positioning Z	50 μm
tip / tilt	0.1 degrees
tip/tilt of the detector	0.9 degrees

Table 3. Tolerancing results

Nominal RMS spot radius (field averaged)	6.15 μm
Mean RMS spot radius	13.5 μm
standard deviation	9.06 μm
X FPA decenter standard deviation	152 μm
Y FPA decenter standard deviation	60.4 μm
focus standard deviation	191 μm

5.3. Manufacturing of the αZ configuration design

As the system has been designed without alignment capabilities, the manufacturing tolerances had to be reduced as much as possible. The solution chosen was to manufacture the structure using 5 axes machining as shown in Fig. 7 (b).

The mirrors have been manufactured using diamond turning. More details on diamond turning and other manufacturing techniques for freeform optics are given in article from Fang et al. [25]. The blanks of the mirrors is visible in Fig. 7(a) and the manufacturing of the third mirror is shown in Fig. 7(c). In Fig. 7(d), a cross section of the mechanical part of the instrument has been manufactured using 3D printing to show the inside of the design, and particularly the position of the mirrors and the baffle shape designed to limit the straylight. The end result is shown in Fig. 8. Mirrors are positioned inside the mechanical mount using a shrink fit method.

Optics EXPRESS

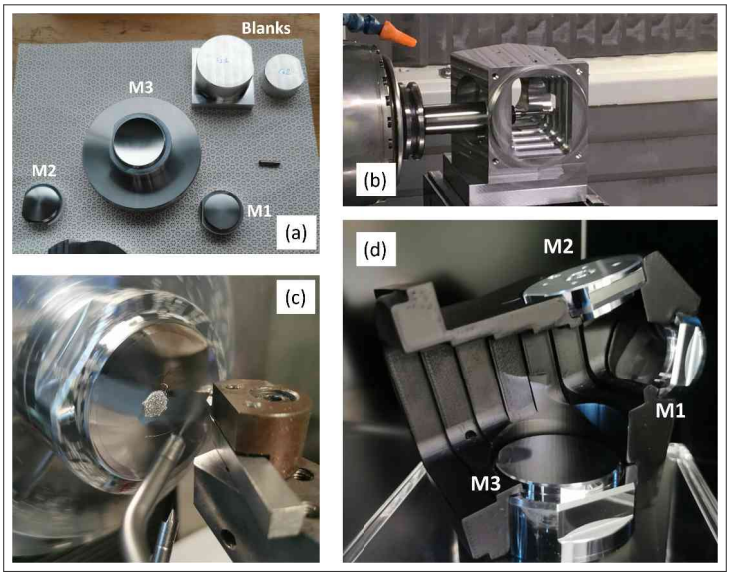

Fig. 7. (a) Blanks of the three freeform mirrors of the αZ prototype. The two block marked G1 and G2 are blanks for the final mirrors. (b) Manufacturing of the mechanical structure of the αZ prototype using 5 axis machining. (c) Diamond turning of the third mirror of the αZ prototype. (d) cross-section of the design.

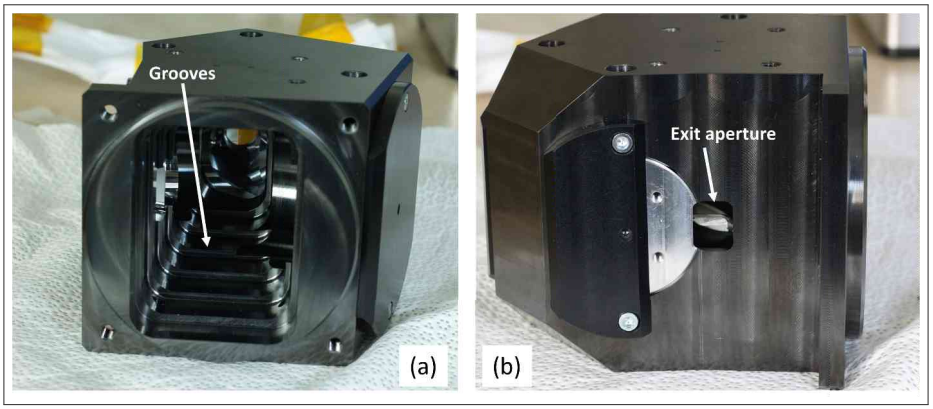

Fig. 8. (a) Entrance aperture of the finished design. (b) Exit aperture of the finished design.

6. Characterization of the prototype of the αZ configuration design

6.1. Bench setup

The principal bench setup used for the characterization of the design is shown in Fig. 9. A cavity blackbody is used for the thermal infrared source. The point source is a pinhole of 500 μm diameter in the focal plane of a 2m focal length collimator. The prototype is placed on a mechanical cradle that is used to perform analyses over the whole field of view.

Optics EXPRESS

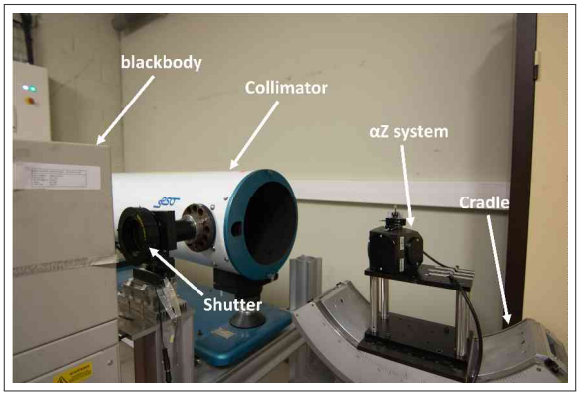

Fig. 9. setup of the characterization of the alpha-Z prototype.

6.2. *First infrared images*

The detector is an ATTO 640 from Lynred. Raw images taken by an uncooled microbolometer are very noisy. Each pixel in the array has an unique response, supposedly linear, with an unique gain and offset. A first correction of the image is made by a one point non uniformity correction (NUC), that corrects only the offset for each pixel. This correction is done by measuring first an uniform planar blackbody. Figure 10 show an example picture obtained with the αZ prototype.

Fig. 10. Image obtained using the microbolometer with a 1pt NUC. Mean of 20 images at 30 fps.

6.3. *Optical quality measurement*

The goal of this prototype was to demonstrate first the capabilities of such instrument in the thermal infrared domain. To assess the optical quality of an optical system we chose to measure the point spread function via spot scan, also called microscanning. The spot scan method is a method to reconstruct the point spread function with subpixel resolution using only one pixel.

Optics EXPRESS

This method consist in generating a point spread function on the detector using a collimated light source as described in section 5.1. Then, the PSF is moved over the pixel of interest by rotating the instrument. The rotation is made with small increments, leading to movements of the PSF of less than a pixel in the image space. This method allows to obtain the PSF of the system with subpixel resolution and using only one pixel with constant gain and offset. The modulation transfer function (MTF) is then obtained via Fourier transformation of this PSF. This MTF is then compared to a theoretical limit computed using the nominal MTF of the design multiplied by the MTF of a square 12μm pixel (Lynred ATTO 640 thermal imaging sensor) and the MTF of the source pinhole, considered as a small circle. The method is similar to the one used in article from Nghiem et al. [26].

Figure 11 presents the PSF and the associated MTF of the system for several object fields. In some of the figures, the MTF is sometimes higher than the diffraction limit. This effect is due to measurement uncertainties such as the precision of the mechanical stages.

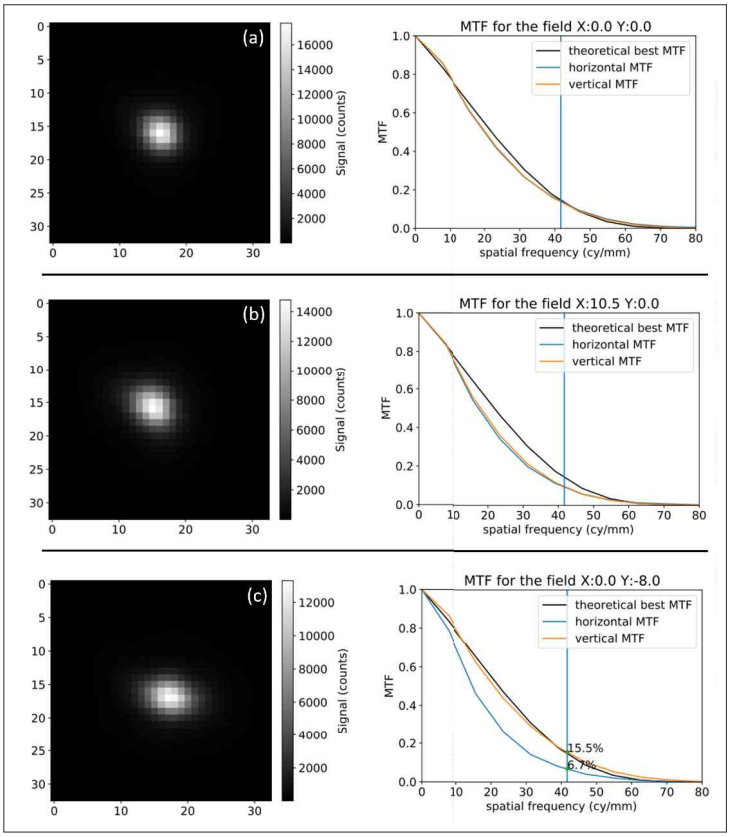

Fig. 11. (a) PSF and MTF for the center field. (b) PSF and MTF measured for a field of 10.5 degrees over the X axis. (c) PSF and MTF measured for a field of -8 degrees over the Y axis. PSF images axes are in pixels (of the oversampled image).

As shown in Fig. 11 (a), the system is diffraction limited on axis. In sub figure (b) it appears that the MTF is only slightly reduced for large field of views over the X axis. In subfigure (c) the MTF is reduced in one direction. This optical quality is compliant with the toleranced optical quality and is very satisfying regarding the limited set of compensators (limited to the position of the detector).

Optics EXPRESS

6.4. Noise equivalent temperature difference

The Noise Equivalent Temperature Difference (NETD) is defined as the smallest temperature variation that induces a signal change equal to the noise, i.e. a SNR of 1, and thus that can be detected with the instrument. The NETD of each pixel p is defined as:

$$NETD_p = \frac{\sigma_S}{\frac{\Delta_S}{\Delta_{T_{CN}}}} \tag{1}$$

With σ_S the temporal noise, Δ_S the variation of the mean signal due to a temperature variation of $\Delta_{T_{CN}}$. As those data are measured, the NETD depends on the choice of the temperature used to measure the noise and the temperature variation chosen. To perform this calculation, the data used are from the measurement inside a climatic chamber used to stabilize the temperature of the system. For each blackbody temperature, one hundred images have been taken. From these images we can compute the mean value of each pixel and the standard deviation around this value, allowing for a fine measurement of the NETD. Here, we chose to use the noise of the measurements at a blackbody temperature of $25°C$, and calculated Δ_S with a variation of T_{CN} from 25 to $30°C$. For this instrument, the mean NETD is $105mK$ with a variance of $\sigma_{NETD} = 0.1mK$. The detector ATTO640 was given with a NETD inferior to 60mK at 300K and with an F/1 aperture. As the NETD varies with the square of the F number, it would correspond to a 135mK NETD at a F/1.5 aperture, which is compliant with the results of our study.

6.5. Distortion

The system presents distortion, as expected from the design. In the process, distortion and focal length are constrained at the same time, via constraint on the real position of the centroid. To test the distortion of the design, a grid of points has been imaged. The whole field of view is sampled into an evenly spaced grid. For each object angle, an image is taken with a one point non uniformity correction and the centroid of the PSF is computed. The overall maximum useful signal S_{max} value is found and for each image i, the maximal value of the image $S_{max,i}$ is compared to S_{max} so that any image where $S_{max,i} < S_{max}/10$ is ignored. This filters out the images where there is no visible PSF, whether it is due to an error of the shutter that did not open or due to the fact that the field angle is too large and the PSF is imaged outside of the detector. The grid of the centroid positions in the focal plane is plotted in red in Fig. 12 (a). This grid is compared to a theoretical grid, in blue, that would be generated by a perfect lens. The equivalent focal length of the system is then the focal length of the perfect lens that gives the blue grid closest to the red grid. This calculation is done via least square minimization of the difference between the two grids. The distortion is computed from the difference between both grids. With a focal length of 18.22mm, and a distortion of 6%, the results are coherent with the design properties. A second verification is made by comparing directly the measured grid to the distortion grid given by the optical design software. The resulting image is shown in Fig. 12 (b), with the measured grid still in red. The measured distortion grid is almost identical to the design grid, meaning that the magnification and distortion of the prototype are exactly as designed. The distortion of the design can be corrected with image processing.

6.6. Straylight

The configuration has been developed to create a design that has a large field of view using only freeform mirrors while removing any specular straylight. Nevertheless, the prototype presents a visible straylight path that creates a straylight spot on the detector for a source located at about 25 degrees Y. The spot is visible in Fig. 14(a). The figure shows a straylight spot that was not anticipated in the design process. We can deduce that this straylight is due to a diffuse or specular straylight on the opto-mechanical structure of the TMA. The shape of the spot is typical of

Optics EXPRESS

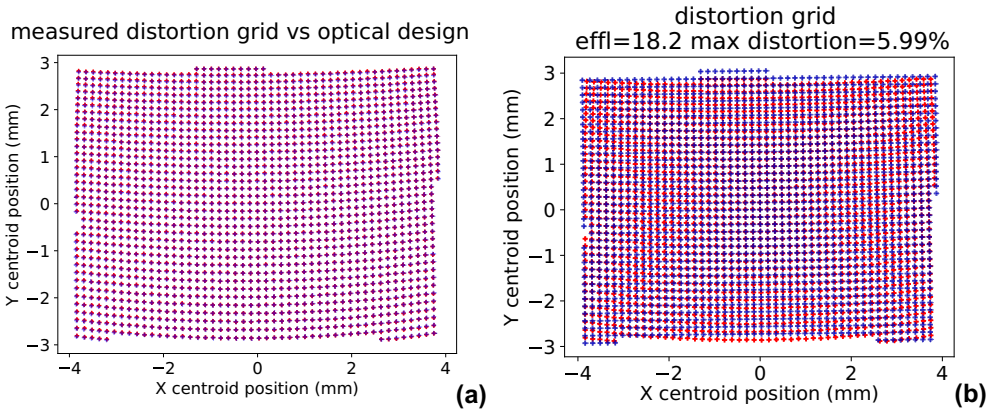

Fig. 12. (a):Measure of the distortion and focal length of the αZ prototype, by comparing the measured distortion grid (red) with a reference grid (blue) with no distortion. (b):Comparison between the measured distortion grid (red) and the expected distortion grid (blue) extracted from the optical design software.

those given by a quasi specular reflection on a mechanical part. The mechanical part has been added into the non sequential design system. To account for quasi specular reflexions hitting the detector, a source has been placed onto the detector and an ideal coating has been applied to the whole mechanical structure. This coating induces a scattering and the BRDF chosen is a narrow gaussian distribution. Multiple reflections onto the mechanical structure are neglected due to the absorption and scattering of the surface. When we trace only rays that are scattered once with an incidence angle larger than 60 degrees and leaving the system, we observe a straylight path for an object placed at a 25 degrees incidence angle (Fig. 13).

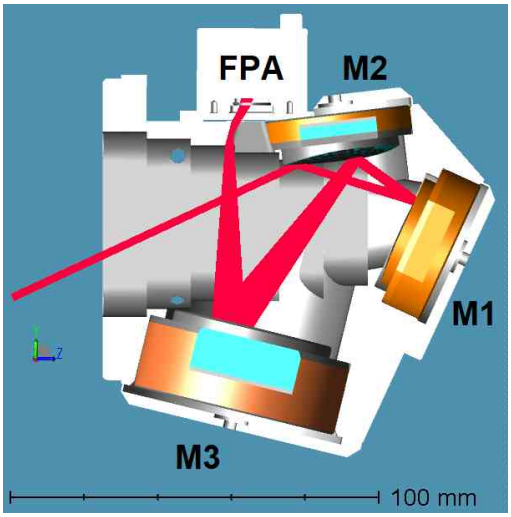

Fig. 13. Straylight path of the αZ design.

The straylight path identified is the path M2-M1-M2-M3 followed by a quasi specular reflection on the mechanical structure. A ray tracing simulation has been made to ensure that this is the problematic straylight route. A collimated beam with a 25 degrees angle has been simulated and the resulting image on the detector is given in Fig. 14(b). The Figure shows a similar pattern,

Optics EXPRESS

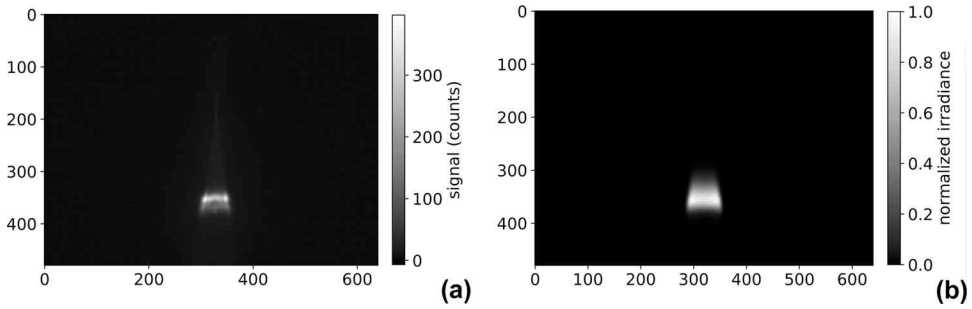

Fig. 14. (a):Straylight spot generated by a collimated source at 25 degrees. (b):Simulated image of straylight from a source located at a 25 degrees angle. Image is the normalized irradiance on the detector.

even with an approximative scattering model, ensuring that the straylight path has been correctly identified. While this path was difficult to anticipate, it is also a rather simple straylight path to fix by adding a step design on the structure close to the detector to avoid such a specular reflection.

7. Conclusion

Freeform surfaces allow to explore a wider range of configurations that could not be viable with only rotationally symmetric surfaces. In this article, we have studied the interest of configuration of mirrors in a circle to increase the field of view of a catoptric system. We designed a fast pamplemousse and a fast αZ systems, both with a field of view of 18x24 degrees and a F number of 1.5. We demonstrate that the αZ geometry has better straylight management than the pamplemousse solution. For large field of view and large aperture designs where straylight must be managed, the αZ geometry should therefore be considered. A prototype of this geometry have been designed and manufactured without alignment capabilities to show that such designs are compatible with fast integration processes. Such processes are important for industrial production of these systems, as the alignment phase is time consuming. Finally, this prototype has been characterized and shows good overall optical quality in the LWIR domain using an uncooled microbolometer array. The back focus is also larger in the αZ design compared to the pamplemousse design leaving enough space to insert a dichroic filter, paving the way for a multispectral camera. This geometry is particularly compact and has already an adequate spherical allocated volume for optronic pods embarked in small aircrafts such as drones.

Funding. Office National d'études et de Recherches Aérospatiales; Agence de l'innovation de Défense.

Acknowledgment. The authors would like to thank Optique et Microsystémes (Opμs) for the manufacturing of the mechanical structure and Gaggione for the mirrors. The authors would also like to thank the anonymous reviewers for their insightful comments and suggestions that helped improve the paper.

Disclosures. The authors declare no conflict of interest.

Data availability. Data underlying the results presented in this paper are not publicly available at this time but may be obtained from the authors upon reasonable request.

References

1. J. P. Rolland, M. A. Davies, T. J. Suleski, C. Evans, A. Bauer, J. C. Lambropoulos, and K. Falaggis, "Freeform optics for imaging," Optica **8**(2), 161 (2021).
2. K. P. Thompson and J. P. Rolland, "Freeform optical surfaces: a revolution in imaging optical design," Opt. Photonics News **23**(6), 30 (2012).
3. K. Fuerschbach, J. P. Rolland, and K. P. Thompson, "A new family of optical systems employing phi-polynomial surfaces," Opt. Express **19**(22), 21919 (2011).
4. E. M. Schiesser, A. Bauer, and J. P. Rolland, "Effect of freeform surfaces on the volume and performance of unobscured three mirror imagers in comparison with off-axis rotationally symmetric polynomials," Opt. Express **27**(15), 21750 (2019).

Optics EXPRESS

5. L. G. Cook, "Three mirror anastigmatic optical system," (1981).
6. J.-B. Volatier, L. Duveau, and G. Druart, "An exploration of the freeform two-mirror off-axis solution space," JPhys Photonics **2**(1), 014004 (2020).
7. J. Zhu, W. Hou, X. Zhang, and G. Jin, "Design of a low F-number freeform off-axis three-mirror system with rectangular field-of-view," J. Opt. **17**(1), 015605 (2015).
8. A. Bauer, E. M. Schiesser, and J. P. Rolland, "Starting geometry creation and design method for freeform optics," Nat. Commun. **9**(1), 1756 (2018).
9. J. C. Papa, J. M. Howard, and J. P. Rolland, "Three-mirror freeform imagers," in *Optical Design and Engineering VII*, L. Mazuray, R. Wartmann, and A. P. Wood, eds. (SPIE, Frankfurt, Germany, 2018), p. 43.
10. G. Huby, R. P. Kleihorst, K. Mellab, and L. Grignard, *Proba-v, a vegetation satellite*, (Toulouse, France, 2010), p. 78260R.
11. R. Geyl, E. Ruch, H. Leplan, S. Lopez, and F. Riguet, "Freeform optics design and manufacturing for microcarb," in *Optical Fabrication, Testing, and Metrology VI*, S. Schröder and R. Geyl, eds. (SPIE, Frankfurt, Germany, 2018), p. 9.
12. L. Duveau, T. Lépine, E. Hugot, X. Briottet, and G. Druart, "Design strategies of an unobscured three mirror telescope with freeform surfaces for infrared nanosatellite imagery," in *International Conference on Space Optics - ICSO 2020*, Z. Sodnik, B. Cugny, and N. Karafolas, eds. (SPIE, Online Only, France, 2021), p. 11.
13. Q. Meng, H. Wang, W. Liang, Z. Yan, and B. Wang, "Design of off-axis three-mirror systems with ultrawide field of view based on an expansion process of surface freeform and field of view," Appl. Opt. **58**(3), 609 (2019).
14. G. Cook, "Wide field of view focal three-mirror anastigmat," (1992).
15. T. Nakano and Y. Tamagawa, "Configuration of an off-axis three-mirror system focused on compactness and brightness," Appl. Opt. **44**(5), 776 (2005).
16. K. Fuerschbach, G. E. Davis, and K. P. Thompson, *Pamplemousse: The optical design, fabrication, and assembly of a three-mirror freeform imaging telescope*, (Kohala Coast, Hawaii, United States, 2014), p. 92930L.
17. K. Fuerschbach, G. E. Davis, K. P. Thompson, and J. P. Rolland, "Assembly of a freeform off-axis optical system employing three \varphi-polynomial Zernike mirrors," Opt. Lett. **39**(10), 2896 (2014).
18. D. Zhu, Z. Hu, J. Yan, Z. Xu, A. Cao, and J. Su, "Design of a compact off-axis freeform three-mirror system in a circular configuration," Appl. Opt. **61**(24), 7078 (2022).
19. I. Trumper, A. Q. Anderson, J. M. Howard, G. West, and D. W. Kim, "Design form classification of two-mirror unobstructed freeform telescopes," Opt. Eng. **59**(2), 025105 (2020).
20. C. Xu, X. Lai, D. Cheng, Y. Wang, and K. Wu, "Automatic optical path configuration variation in off-axis mirror system design," Opt. Express **27**(11), 15251 (2019).
21. N. Takaki, A. Bauer, and J. P. Rolland, "Degeneracy in freeform surfaces described with orthogonal polynomials," Appl. Opt. **57**(35), 10348 (2018).
22. L. Duveau, C. Freslier, G. Druart, and T. Lepine, "Freeform TMA without planar symmetry for compact catoptric imaging system," Results Opt. **12**, 100434 (2023).
23. A. Bauer and J. P. Rolland, "Roadmap for the unobscured three-mirror freeform design space," Opt. Express **29**(17), 26736 (2021).
24. L. Duveau and G. Druart, "Systeme optique imageur a trois miroirs," (2022). WO2022129770.
25. F. Fang, X. Zhang, A. Weckenmann, G. Zhang, and C. Evans, "Manufacturing and measurement of freeform optics," CIRP Ann. **62**(2), 823–846 (2013).
26. J. Nghiem, J. Jaeck, J. Primot, C. Coudrain, S. Derelle, E. Huard, M. Caes, S. Bernhardt, R. Haidar, P. Christol, and I. Ribet-Mohamed, "Mtf measurements of a type ii superlattice infrared focal plane array sealed in a cryocooler," Opt. Express **26**(8), 11034 (2018).